Energy Storage Materials 65 (2024) 103148

Contents lists available at ScienceDirect

Energy Storage Materials

journal homepage: www.elsevier.com/locate/ensm

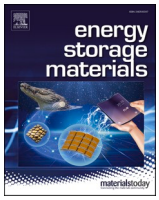

3D networked MXene thin films for high performance supercapacitors

Dahnan Spurling [a,§,*], Helge Krüger [b,§], Niklas Kohlmann [c], Florian Rasch [b], Matthias P. Kremer [a], Lorenz Kienle [c], Rainer Adelung [b], Valeria Nicolosi [a,*], Fabian Schütt [b,*]

[a] School of Chemistry, Centre for Research on Adaptive Nanostructures and Nanodevices (CRANN) & Advanced Materials Bio-Engineering Research Centre (AMBER), Trinity College Dublin, Dublin 2, Ireland

[b] Functional Nanomaterials, Institute for Materials Science, Faculty of Engineering, Kiel University, Kaiserstr. 2, 24143, Kiel, Germany

[c] Synthesis and Real Structure, Institute for Materials Science, Faculty of Engineering, Kiel University, Kaiserstr. 2, 24143 Kiel, Germany

ARTICLE INFO

Keywords:
Mxene
Aeromaterial
Supercapacitor
Energy storage
High areal loading

ABSTRACT

Maximizing the energy and power density of supercapacitors requires thick electrodes, enabling a high areal loading. Simultaneously, a sophisticated, hierarchical pore structure for the active material is needed, granting high accessibility for electrons and ions. However, porosity and thickness need to be carefully balanced to maximize the active material density while ensuring high performance. Here, we show that by forming hierarchical electrodes from $Ti_3C_2T_x$ 2D nanosheets in the form of interconnected 3D networked thin films (up to ~220 nm), we can fabricate high performance thick film electrodes of up to ~50 μm with a well-defined, hierarchical, porous structure. By balancing porosity and thickness, we demonstrate electrodes that combine a high areal loading of up to ~7.2 mg cm^{-2}, high material density of ~1440 mg cm^{-3}, and high electrochemical performance of 240 F g^{-1} and 140 F cm^{-3}. Thus, we achieve electrodes with a remarkable areal capacitance of ~1.4 F cm^{-2}, even at high rates of 200 mV s^{-1}, outperforming other state of the art MXene based electrodes of comparable density and thickness. We anticipate that this concept, will pave the way to transfer the exceptional properties of nanomaterial thin film electrodes to the next, macroscopic level, enabling the development of advanced, high-performance electrodes for practically relevant energy storage applications and beyond.

1. Introduction

The global appetite for energy storage is growing at an astounding rate [1], the often-conflicting goals of sustainability and economic growth being the key drivers. As the prevalence of portable electronics, electric vehicles, and intermittent energy sources such as wind and solar increases, so too does the demand for efficient short- and long-term energy storage.

Supercapacitors, as one of the most promising short-term energy storage devices, store charge through physisorption of ions on the surface of the electrode or by fast, surface-confined faradaic charge transfer. Both processes are kinetically fast in contrast to intercalation in batteries, granting them high power density and cycle stability at the expense of energy density [2].

In this context, nanostructured electrode materials such as graphene [3], carbon black [4], or MXene [5] are particularly attractive for high-performance supercapacitor electrodes due to their high conductivity, large surface area, and redox-active sites. In particular, ultrathin (< 100 nm) MXene electrodes show excellent gravimetric capacitance and rate performance of up to 450 F g^{-1} at 100 V s^{-1} [6]. However, for practical applications, high energy and high power density are required, meaning that the active material areal loading must be maximized in order to proportionally reduce the weight of passive components (housing, current collectors, etc.) [7,8]. A high areal loading (up to 10 mg cm^{-2}) requires thick electrodes, but the nanostructured electrode materials must retain as much of their theoretical capacitance and rate performance as possible [7]. Conventional methods to fabricate thick films of nanostructured materials (see Fig. 1, top route) show a drastic decrease in performance due to a compact layered structure. This leads to long, meandering diffusion paths that strongly inhibit ion transport, limiting both the response time and the accessible surface area of the electrode. Recently, dense electrodes have been prepared through gelation and spacing [9], partially ameliorating this issue and achieving very high areal capacitance of 18.6 F cm^{-2}.

* Corresponding authors.
E-mail addresses: spurlind@tcd.ie (D. Spurling), nicolov@tcd.ie (V. Nicolosi), fas@tf.uni-kiel.de (F. Schütt).
§ These authors contributed equally to this work

https://doi.org/10.1016/j.ensm.2023.103148
Received 20 July 2023; Received in revised form 8 December 2023; Accepted 18 December 2023
Available online 20 December 2023

However, the extreme density of this structure still leads to poor overall rate performance, losing 75 % of its specific capacitance when increasing scan rate from 2 to 100 mV s^{-1}. To circumvent this, a sophisticated, hierarchical pore structure is a prerequisite to provide efficient transport for electrons and ions. Although several methods have been suggested, including vacuum-filtering [6], freeze drying [10], hydrogels/clays [6,11], vertical alignment [12], and 3D printing [7], none of have been able to achieve an electrode that adequately combines the properties of strong gravimetric, areal, and volumetric capacitance at high scan rates.

In this work, we demonstrate that high areal capacitance as well as high charge and discharge rates can be achieved simultaneously *via* a versatile template-based fabrication method for the synthesis of thick electrodes (> 50 μm) composed of 3D networked MXene thin films (< 220 nm). This method enables versatile tuning of both the microstructure and nanostructure of the thick electrode in a controlled manner, optimizing the areal mass loading and density without sacrificing surface accessibility or short ion diffusion pathways (see Fig. 1, bottom route).

Tunable nanostructure and areal loadings can be achieved through varying the 3D networked MXene thin films' thickness (from 70 nm-220 nm), and tunable microstructure through nondestructive compression to down to ~50 μm. In this way, supercapacitor electrodes with areal loadings of up to 7.2 mg cm^{-2} and densities up to 1440 mg cm^{-3} are achieved. At high charge and discharge rates of 200 mV s^{-1} these 3D networked MXene thin film electrodes display gravimetric and volumetric capacitances of 210 F g^{-1} and 140 F cm^{-3} respectively. Additionally, in optimally configured electrodes, a remarkable capacitance of ~ 1.4 F cm^{-2} (at 200 mV s^{-1}) can be achieved, greater than similarly dense and thick MXene electrode systems [6,11,12], which remain benchmarks in 2D material energy storage.

2. Results and discussion

2.1. Fabrication of 3D networked MXene thin films

Here we show that micrometer-sized $Ti_3C_2T_x$ MXene flakes (see Figure S 1a) produced from a top-down etching technique can be formed into 3D networked 2D material thin film structures by using a sacrificial template-based approach. We found that by using this process, the areal loading of the electrode can be tuned (from ~2 mg cm^{-2} > ~7 mg cm^{-2}) while simultaneously adjusting the individual layer thickness of the hierarchical structure (70 nm – 220 nm) (see Fig. 2).

The $Ti_3C_2T_x$ used is of high quality (see Fig. S1), with large flakes, dark green colloidal dispersions and forming freestanding filtered films. XRD of such a film can be seen in Fig. S 2, with characteristic (0 0 l) reflections and complete removal of Ti_3AlC_2 reflections. The (0 0 2) reflection at 7.07° corresponds to a d-spacing of 12.5 Å, and interlayer spacing of 3.1 Å, based on a dry multilayer spacing of 9.4 Å [13,14].

The process for preparing the 3D networked MXene thin film structures (AMX) is schematically shown in Fig. S 4a. In short, a highly porous (~94 %) ceramic template consisting of interconnected tetrapodal-shaped ZnO (t-ZnO) microparticles (Figure S 5 a, b, c) is infiltrated with a water-based dispersion of MXenes (Supplementary Video 1, for details about the dispersion, see Figure S 1). The specifics of this infiltration process have been reported for other materials elsewhere [15–17]. For this work, AMX with a cylindrical geometry (12 mm diameter and 2 mm height) was employed, but other template geometries can be used, as shown in Figure S 5a. The as-produced AMX structures consist of a network of interconnected hollow microtubes with a mean length of ~25 μm and a diameter of ~2 μm, as shown in Figure S 6d-f. While both the diameter and length of the tubes are fixed, it was found that the wall thickness of the MXene microtubes can be adjusted between ~70 nm and ~220 nm by varying the number of successive MXene depositions, as illustrated in Fig. 2e-i. The lowest achievable wall thickness of ~70 nm is AMX-4D-2000 (D indicating the

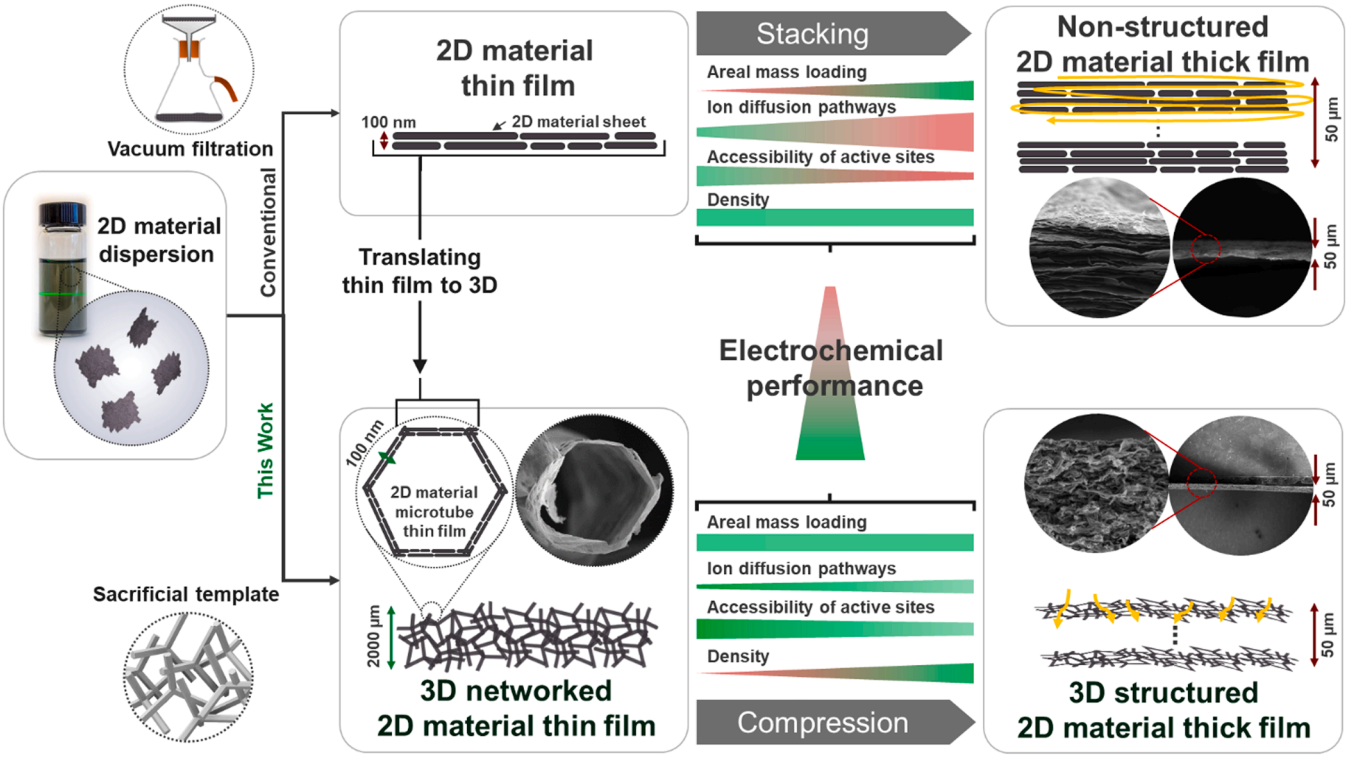

Fig. 1. Comparison between conventional methods for the fabrication of 2D material thick film electrodes, e.g., by vacuum filtration (top route), and the here demonstrated concept for the fabrication of 3D networked 2D material thin films (bottom route), highlighting the change in the electrochemical performance of the electrodes by stacking or compression, respectively.

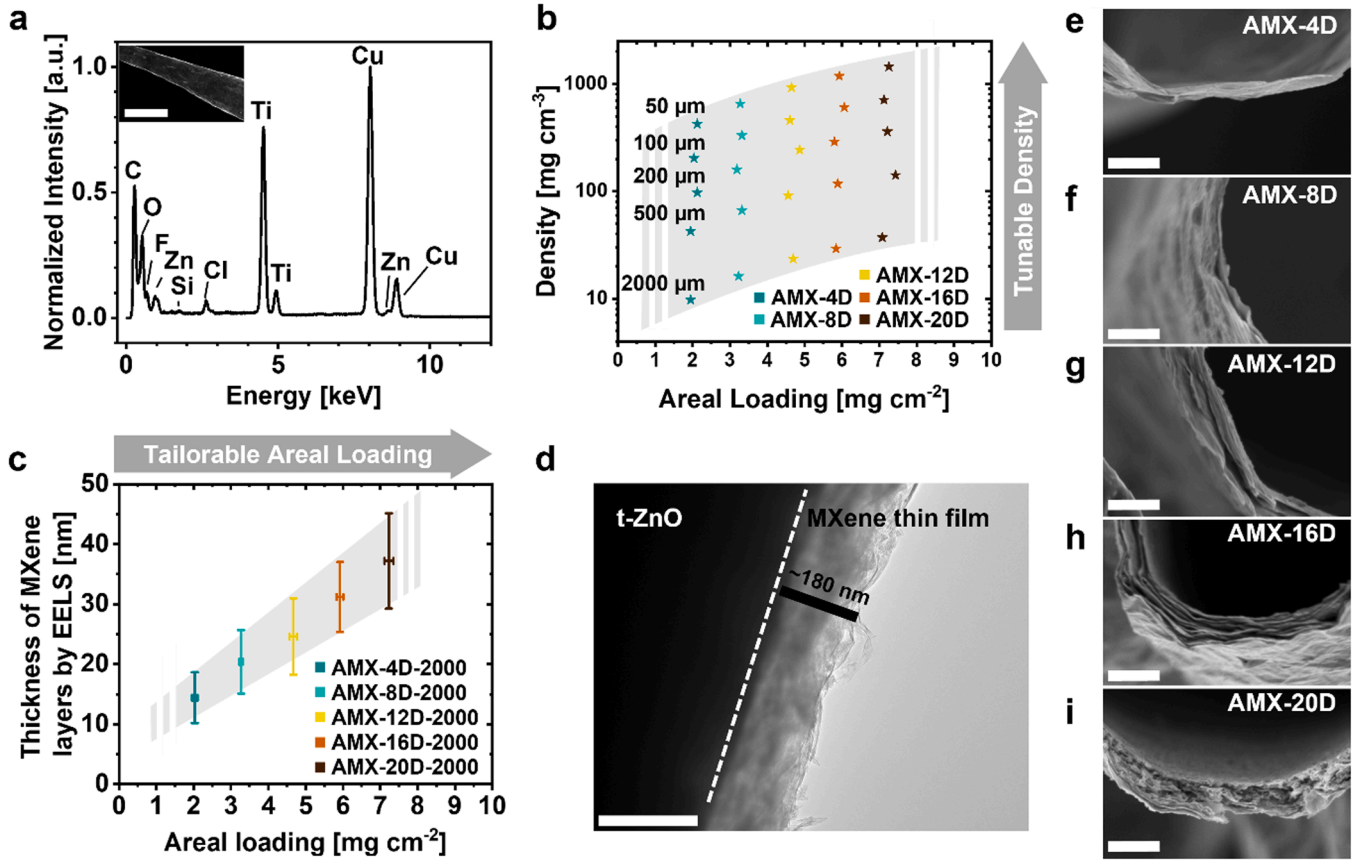

Fig. 2. (a) EDX spectrum recorded by scanning across an AMX microtube after template removal (see inset, scale bar 4 µm) showing that no (ZnO) is present. (b) Density and area loading of various prepared AMX structures showing the versatility of the approach used, with the gray area denoting the region of possible electrodes and the stars denoting the prepared samples. (c) Layer thickness of the differently prepared AMX structures with tailored nanostructure determined by STEM EELS line scans across individual AMX tubes. (d) Bright field image of an AMX-16D before t-ZnO etching showing the effective film thickness on the t-ZnO surface (scale bar 200 nm), including pores or gaps between MXene flakes. (e-i) SEM images of AMX-4D-2000, AMX-8D-2000, AMX-12D-2000, AMX-16D-2000, AMX-20D-2000, each looking at a free-standing MXene microtube, showing the increase in wall thickness due to the deposition process used (scale bar: 400 nm).

number of MXene depositions and 2000 indicating the overall thickness in µm), while AMX-20D-2000 corresponds to the highest studied wall thickness of ~220 nm (details of the structure see Fig. S 7). These structures showed a tailorable areal loading between ~2 and ~7.2 mg cm^{-2}.

Interestingly, we also show that these electrode structures can be tuned through controlled compression, increasing density with respect to the as-prepared structure up to 40 times, e.g., by compressing a 2 mm thick AMX structure (AMX-4D-2000) non-destructively to a thickness of 50 µm (AMX-4D-50) (see Fig. S 8) [18]. This controlled compression enables a range of volumetric densities from ~10 to ~1440 mg cm^{-3}.

2.2. AMX electrode design for tunable nano and microstructure properties

The nanostructure of the AMX material was characterized using advanced transmission electron microscopy (TEM) techniques. The sum spectra of energy dispersive X-ray (EDX) measurements (Fig. 2a) indicate removal of the sacrificial ZnO scaffold, with only trace Zn peaks remaining, possibly due to Zn^{2+} ions intercalating between the MXene layers as the scaffold is etched. This is reinforced by the disappearance of ZnO reflections from X-ray diffraction (XRD) in the etched AMX sample (see Figure S 3a). The (0 0 2) reflection of the etched AMX at 6.03° corresponds to a d-spacing of 14.7 Å, or interlayer spacing of 5.3 Å [13,14], an increase relative to the vacuum filtered MXene film in Figure S 2, reinforcing the conclusion that there is some intercalation of Zn^{2+} ions between the MXene layers. Furthermore, comparing XRD before and after etching with zero offset (see Figure S 2b) there is no clear introduction of peaks characteristic of anatase TiO_2, namely (1 0 1) at $2\theta = 25.5°$, (0 0 4) at $2\theta = 37.9°$, (2 0 0) at $2\theta = 48.1°$ or (1 0 5) at $2\theta = 54.0°$ indicating minimal oxidation of the AMX structure [19] during overnight etching in 1 M HCl. This is consistent with previous studies, showing that prolonged exposure to acidic pH has a similar effect to neutral conditions on $Ti_3C_2T_x$ [20]. Raman characterization of the AMX electrodes (Figure S 9) clearly show the in-plane vibration peaks attributable to T_x surface groups at approximately 400 cm^{-1} (predominantly OH), 250 cm^{-1}, and 600 cm^{-1} (predominantly O). Out-of-plane vibrations at approximately 200 cm^{-1} and 720 cm^{-1} often measured in $Ti_3C_2T_x$ spectra are suppressed due to intercalated water weakening of coupling between the flakes and additionally due to excitation wavelength in the case of the latter [21].

As described before, the nanostructure, i.e., the wall thickness of the hollow microtubes of the AMX can be tuned by adjusting the parameters of the deposition process. The MXene layer thickness as a function of areal loading is shown in Fig. 2c. The layer thickness was determined by using scanning transmission electron microscopy electron energy loss spectroscopy (STEM-EELS) techniques assuming an inelastic electron mean free path of 105 nm (details can be found in the experimental section and in Figure S 10). As shown in Fig. 2c, there is an almost linear dependence of the MXene microtubes' wall thickness [15,17] from ~11 nm for the AMX-4D-2000 to ~32 nm for the AMX-20D-2000, each deposition step corresponding to an increase in areal loading of ~ 0.3 mg cm^{-2}. The material layer thickness determined via STEM-EELS is the integrated height of solid matter in electron beam direction. Thus, gaps or pores are not considered. The self-organized restacking process of the

MXene flakes during deposition process, however, leads to some porosity within the formed hollow MXene microtubes. Furthermore, the calculated inelastic electron mean free path assumes a densely packed material while MXenes themselves have a layered structure with comparatively large lattice parameters in c-direction. Consequently, TEM bright field images (Fig. 2d and Figure S 11) and scanning electron microscopy (SEM) images (Fig. 2e-i) show a higher (effective) wall thickness of the hollow MXene microtubes compared to the thicknesses from EELS analysis. The coarse layer, or effective, microtube wall thickness thus determined (Figure S 11 and Figure S 12) is in the order of ~70 – 220 nm for the AMX-4D-2000 and AMX-20D-2000 respectively. In addition to the neglection of porosity, the wall thicknesses determined by the EELS log ratio method must be considered as a lower boundary as the calculated electron mean free paths are often smaller than experimental data in the case of high energy electrons in TEM [22].

As previously mentioned, the microstructure and thus, the density of the AMX can be tuned by compression. By controlling both the compression and depositions, the density of the AMX can be tuned by orders of magnitude from ~10 mg cm^{-3} – ~1440 mg cm^{-3} while at the same time the areal loading is adjustable from ~2 mg cm^{-2} - ~7.2 mg cm^{-2} (Fig. 2b and c). In summary, the fabrication process presented here enables highly customizable multi-scale 3D electrode structures comprised of 2D nanomaterials.

2.3. Tunable nanostructure by successive deposition of MXene for high areal performance

The electrochemical performance of the AMX supercapacitor electrodes was evaluated in a three-electrode configuration using 0.5 M H_2SO_4 aqueous electrolyte (setup see Figure S 13a, b). AMX electrodes with tailored nanostructure ($4 < D < 20$), each compressed 10 times to ~200 μm height (initial height = 2000 μm), were investigated. Fig. 3a shows the CVs from 5 mV s^{-1} to 1000 mV s^{-1} of an AMX-16D-200 (others see Figure S 14a, c, e, g and i) indicating typical shape for $Ti_3C_2T_x$, combining the rectangular shape at potential extremes of EDLC with peaks indicative of pseudocapacitance [6,23,24]. The peaks at around –0.45 V (vs. Ag/AgCl) for 5 mV s^{-1} are assigned to pseudocapacitive reactive groups of the MXene [23]. With increasing scan rate, the oxidation and reduction peaks shift to higher and lower potentials, respectively. However, at 500 mV s^{-1} a clear peak in the oxidation scan is still observable, indicating fast diffusion, which indicates good rate performance. Furthermore, at low scan rates there is a narrow peak-to-peak spacing (< 20 mV at 5 mV s^{-1}) and clear oxidation and reduction peaks. Fig. 3b, c demonstrates the cyclic voltammetry (CV) curves of AMX with different microtube wall thicknesses (AMX-4D-200 to AMX-20D-200), at scan rates of 10 mV s^{-1} and 200 mV s^{-1}. [17,37,38] As expected from the increase in mass with increasing microtube wall thickness, peak current approximately doubles from AMX-4D-200 to AMX-8D-200 and again to AMX-20D-200 (Fig. 3a). Oxidation and reduction peaks are clear, and peak-to-peak separation is on the order of 20 mV in all cases, indicating a highly reversible redox process with small IR drop [25,26]. At 200 mV s^{-1} (Fig. 3c), the aforementioned peak positions are shifted to higher and lower potentials respectively, but are still clearly visible. However, the scaling of the peak current at 200 mV s^{-1} is less linear as the microtube wall-thickness increases.

Similar behavior can be observed in galvanostatic charge and discharge studies, as shown in Figure S 14b, d, f, h, and j. When comparing samples with increasing microtube wall thickness, they show almost identical charge and discharge characteristics, especially at lower current densities between 2 and 20 A g^{-1}, indicating good

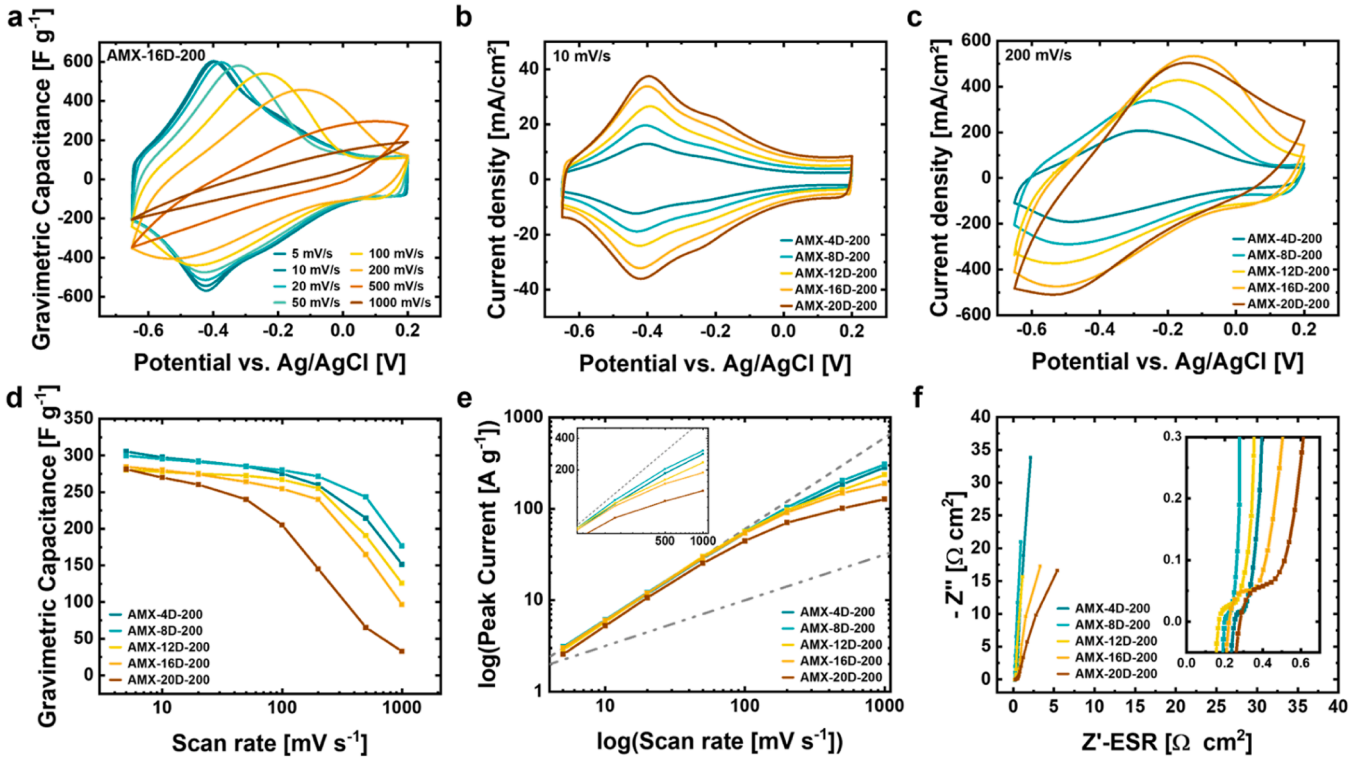

Fig. 3. Electrochemical performance of $Ti_3C_2T_x$ electrodes with tuned nanostructure. (a) Cyclic voltammograms of an AMX-16D-200 with a mass loading of 5.8 mg cm^{-2} in 0.5 M H_2SO_4 at scan rates from 5 mV s^{-1} to 1000 mV s^{-1}. (b) Cyclic voltammograms of different AMX structures with a thickness of 200 μm and weight loading of 2.1 mg cm^{-2}, 3.2 mg cm^{-2}, 4.4 mg cm^{-2}, 5.8 mg cm^{-2} and 7.2 mg cm^{-2} collected at 10 mV s^{-1} and (c) at 200 mV s^{-1}. d) Rate performance of AMX structures with different microtube wall thickness in terms of gravimetric capacitance. (e) Logarithmic representation of the peak current with respect of the scan rate for the determination of the slope, b, for the AMX structures with different microtube wall thickness. Inset is the region of interest above 200 mVs^{-1} where the samples most strongly diverge. (f) Electrochemical impedance spectroscopy collected at 0.2 V vs Ag/AgCl for different AMX structures with an inset showing a detail view of the high frequency area.

capacitance retention and material activation even at high MXene mass loadings. For example, the sum of charge and discharge time at 20 A g^{-1} is 22.46 s, 23.55 s, 19.87 s, 21.10 s and 19.34 for AMX-4D-200, AMX-8D-200, AMX-12D-200, AMX-16D-200, and AMX-20D-200 respectively, showing only small deviations between the samples. Best performance, at 23.55 s, is achieved by the AMX-8D-200 electrode.

Fig. 3d shows the gravimetric capacitance of AMX electrodes as a function of scan rate. For all scan rates, the specific gravimetric capacitance is reduced with increasing microtube wall thickness, e.g., at 100 mV s^{-1} the gravimetric capacitance of AMX-4D-200 is around 280 F g^{-1}, while an AMX-16D-200 electrode is around 250 F g^{-1}. As shown in Fig. 3d, up to 200 mV s^{-1}, the specific gravimetric capacitance only decreases slightly for all electrode configurations. At higher scan rates (>200 mV s^{-1}) the gravimetric capacitance decreases strongly with increasing microtube wall thickness, resulting in progressively poorer capacitance retention. AMX-8D-200 stands out with 50% capacitance retention at 1000 mV s^{-1}, whereas AMX-16D-200 retains only 35% capacitance at the same scan rate. This difference is also visible in Figure S 14, showing the CVs for all other AMX, where AMX-8D-200 has consistently smaller peak-to-peak separation than the other samples, and retains a visible oxidation peak even at 1000 mV s^{-1}. It is expected that at higher scan rates, thicker microtube walls will restrict ion transport in the electrode, however, as mentioned previously, increased wall thickness is also expected to reduce the internal resistance of the electrode, manifesting in greater overall current and a smaller shift in redox peak potentials. These two properties are optimized for the AMX-8D-200 sample, neither too thick for significant diffusion limitation, nor too thin for poor conductivity.

In CV measurements, the peak current, i_p is comprised of current associated with double layer capacitance and fast faradaic reactions on the surface, i_{cap}, and slow, diffusion-limited processes i_{diff} [27]. To analyze the effect of increased microtube wall thickness on the charge storage kinetics more robustly in each electrode, a power law dependence of peak current on scan rate may be assumed [28]:

$$i_p = i_{cap} + i_{diff} = a\nu^b$$

where ν is the scan rate, and a and b are variables. The linear dependence of i_{cap} on ν means that $b = 1$ for systems in which i_p is entirely dependent on capacitive processes, whereas for entirely diffusion-limited systems $b = 0.5$ due to the square root dependence of i_{diff} on ν [29]. In Fig. 3e it can be seen that in all samples, $b \approx 1$ up to 100 mV s^{-1}, though a divergence after this point is observed in the thicker samples, trending towards $b = 0.5$ at a higher rate. This more diffusion limited behavior indicates that the increased conductivity associated with very thick microtube wall thickness cannot compensate for the longer ion diffusion paths of the same at high scan rates. The inset in Fig. 3e indicates a slight decrease in the slope of AMX-8D-200 with respect to AMX-4D-200 above 500 mV s^{-1}, revealing that the AMX-8D-200 sample is indeed more diffusion limited, however this is compensated for by its larger peak current density, supporting the conclusions from Fig. 3d. Furthermore, as seen in the inset electrochemical impedance spectroscopy (EIS) plot in Fig. 3f, the overall internal resistance initially decreases with the number of depositions, but the electrodes clearly become more diffusion limited above AMX-12D-200, with an increasingly less vertical slope in the low frequency region. The EIS spectra were fit according to the circuit inset in Figure S 15a, which shows the fitting of AMX-20D-200. From this fitting, the charge transfer resistance, R_{CT} could be calculated, which shows a slight decrease from AMX4D-200 to AMX-8D-200, followed by a marked increase thereafter (see Figure S 15b). This scaling of R_{CT} supports observations of diffusional limitations in thick microtube walls, and clearly reinforces the conclusion of optimized electrical and ionic properties for AMX-8D-200.

The long-term performance of the AMX-16D-200 sample at a constant current density of 20 A g^{-1} shows a specific capacitance of 261 F g^{-1} at the beginning and 256 F g^{-1} thereafter with almost no loss, supported by a high coulombic efficiency consistently above 99.6 % (see Figure S 17). Moreover, Raman studies after 0, 50, 100, 300 and 5000 cycles (see Figure S 9b) indicate negligible difference in the shape and height of the peaks, which also indicates no change in the structural and chemical properties of $Ti_3C_2T_x$.

Overall, the electrochemical studies clearly demonstrate that increasing the wall thickness of the microtubes and thereby tuning the electrode's nanostructure significantly increases the capacitance per unit area of the electrodes, with optimal rate performance observed for AMX-8D-200.

2.4. Tunable microstructure by compression of electrodes with high volumetric performance

While tuning the microtube wall thickness enables us to optimize the areal loading of the AMX electrodes, the high overall porosity of the initial framework structure (~99.8%) results in a poor volumetric capacitance, e.g., AMX-8D-2000 ~5 F cm^{-3}. As previously discussed, (Figure S 8), the AMX electrodes can be compressed up to 40 times without appreciable loss in structural integrity. To study the effect of the compression on the microstructure and electrochemical performance AMX-8D-2000 electrodes were compressed in thickness to 500 μm (AMX-8D-500), 200 μm (AMX-8D-200), 100 μm (AMX-8D-100) and 50 μm (AMX-8D-50). As demonstrated in Fig. 4a, at low scan rates of 5 mV s^{-1}, the electrochemical performance is not affected at all, indicating a retention of the mechanical and electrical integrity of the electrodes, even at a compression factor of ~40. Furthermore, the absence of changes to redox peak amplitude or overall capacitance implies that for low scan rates, diffusion is sufficiently fast, and that significant restacking or other destruction of ionic pathways has not occurred. At higher scan rates of 200 mV s^{-1}, a clear difference in the electrochemical behavior can be seen as the peak current decreases with increasing compression (Fig. 4b). These indicate that the best rate performance is obtained from AMX-8D-100, with a clearer oxidation peak at a lower potential and greater capacitance overall (Fig. 4c). Indeed, in the case of AMX-8D-50, the oxidation peak is barely visible, and capacitance is on the order of half of that compared to other samples. This points to a disimprovement in diffusional properties, most probably because of the loss in porosity. The overall trend in gravimetric capacitance is shown in Fig. 4d, with AMX-8D-200 exhibiting greater capacitance up to 200 mV/s. The advantage shifts to AMX-8D-100 at 500 mV s^{-1} and above, which retains 93% of its maximum capacitance at 500 mV s^{-1} compared to 80% for AMX-8D-200 and 58% for AMX-8D-50. All AMX-8D samples show purely capacitive-like behavior up to 50 mV s^{-1}, with a value of $b \approx 1$ (Fig. 4e), though a clear divergence after this point is observed in the 50 μm sample, trending towards $b = 0.5$ at a much greater rate.

This more diffusion limited behavior indicates that ion transport is being hindered by the reduction in porosity more than can be compensated for by the reduction in overall thickness of the electrode at such an extreme degree of compression. On the other hand, the slope above 500 mV s^{-1} is marginally closer to 1 for the AMX-8D-100 sample, indicating that diffusion may be slightly aided by the reduced thickness of the electrode, and that the porosity is sufficient for uninhibited ion transport. While gravimetric capacitance is a useful metric to assess how well the active material in an electrode is utilized, real-world devices are more often limited by volume, and this is where tuning the microstructure of AMX electrodes by compression becomes important. Fig. 4f gives an overview of the volumetric capacitance of the AMX electrodes, which at scan rates up to 50 mV s^{-1} scales linearly with the degree of compression. Indeed, even at 50 mV s^{-1}, volumetric capacitance of 180 F cm^{-3} is achieved in the AMX-8D-50 sample. Though diffusional limitations cause a steeper falloff in capacitance at high scan rates with respect to the AMX-8D-100, it only reaches parity at a scan rate of 1000 mV s^{-1}. This represents a discharge time of < 1 s, and would make such an electrode suitable for the plurality of energy storage applications SCs are typically employed in [30,31].

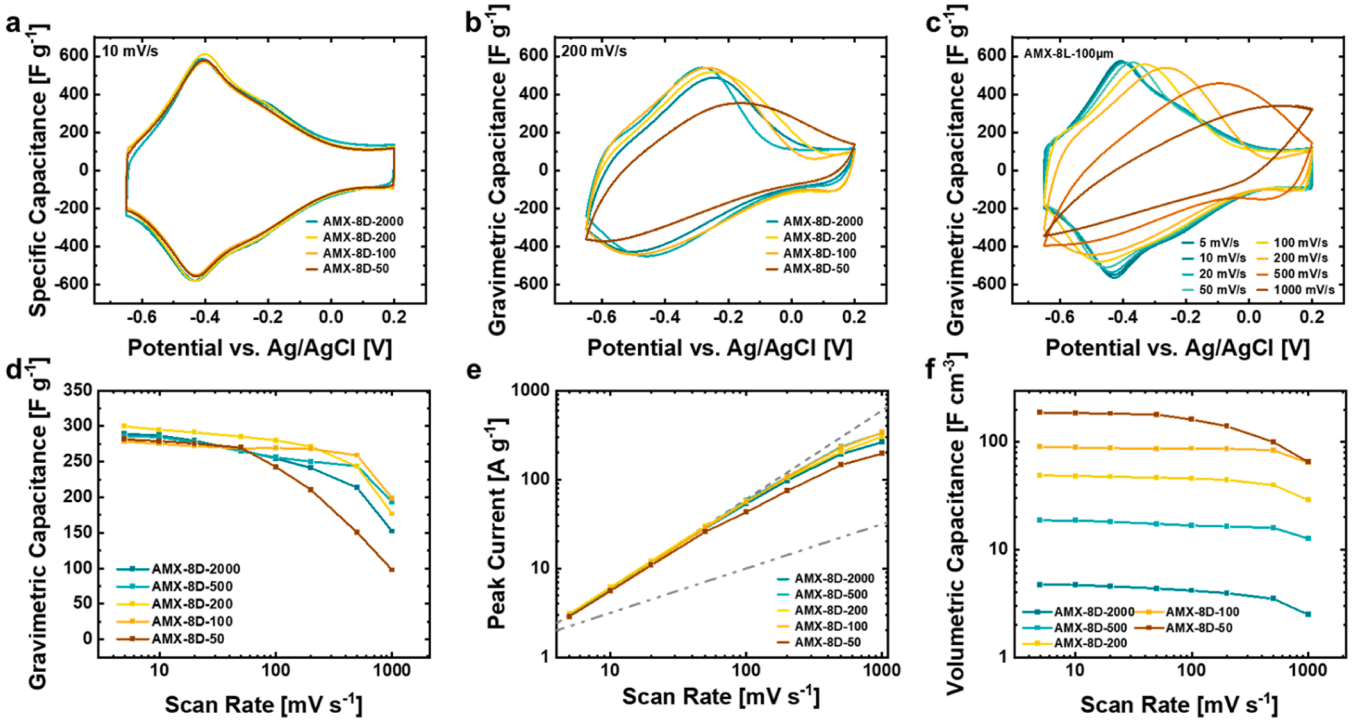

Fig. 4. Electrochemical performance of $Ti_3C_2T_x$ electrodes with tuned microstructure. (a) Cyclic voltammograms of AMX-8D-2000 structures compressed to 500, 200, 100 and 50 μm collected at 10 mV s^{-1}. (a) Cyclic voltammograms of AMX-8D-2000 structures compressed to 500, 200, 100 and 50 μm collected at 200 mV s^{-1}. (c) Cyclic voltammograms of an AMX-8D-100 with a density 323 mg cm^{-3} collected at scan rates from 5 mV s^{-1} to 1000 mV s^{-1}. d) Rate performance of AMX structures with different density in terms of gravimetric capacitance. (e) Logarithmic representation of the peak current with respect of the scan rate for the determination of the slope, b, for the AMX structures with different density. (f) Rate performance of AMX structures with different density in terms of volumetric capacitance.

2.5. *Optimization of gravimetric and volumetric electrode performance*

By addressing both, the nano- and microstructure of the AMX electrodes, their electrochemical performance can be optimized for mass and/or volume depending on the rate performance requirements of the intended application. The relationship between volumetric and gravimetric capacitance at scan rates from 5 to 1000 mV s^{-1} is summarized in Fig. 5a and b for the tunable nano- and microstructured AMX electrodes, respectively. Notably, neither increased compression of the electrode nor increased layer thickness lead to a profound decrease in performance, especially at low scan rates, enabling electrodes with high volumetric and areal capacitance.

Additionally, it is important to note that for commercial SCs, areal capacitance, gravimetric capacitance and density must be considered concurrently. A high areal capacitance improves the packaging of a device by proportionally reducing the amount of supporting material (current collectors, separators) required for the desired overall capacitance.

In terms of the feasibility of 2D nanomaterial-based SCs, gravimetric performance is also vital, as commercially available carbon-based SCs

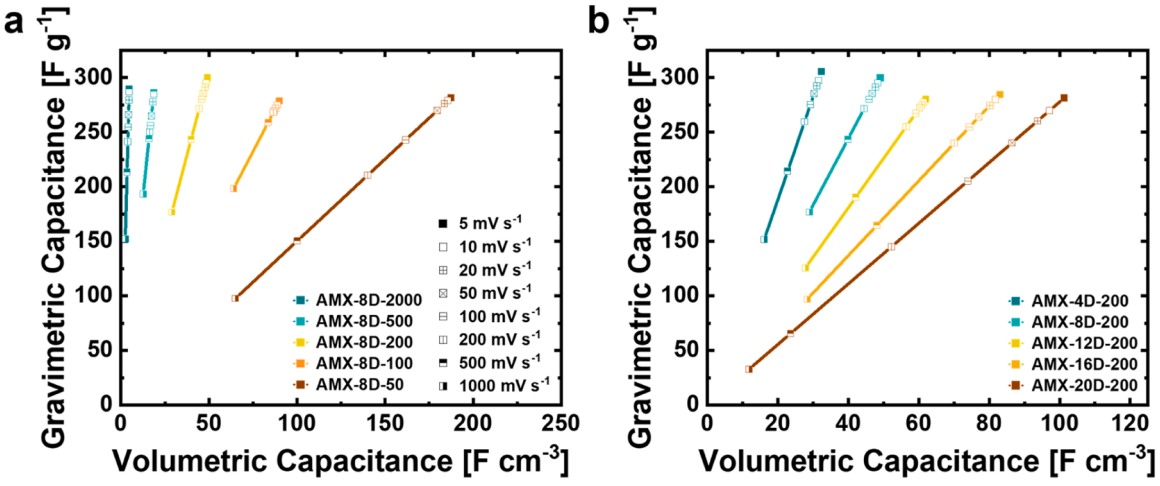

Fig. 5. (a) Relation between gravimetric and volumetric capacitance for 3D networked MXene thin films with tailored microstructure and hence, density, at scan rates from 5 mV s^{-1} to 1000 mV s^{-1}. (b) Relationship between gravimetric and volumetric capacitance for 3D networked MXene thin films with tailored nanostructure and hence, areal loading, at scan rates from 5 mV s^{-1} to 1000 mV s^{-1}.

have relatively low costs associated with the active material. SC-grade activated carbon has a market value in the region of 15 – 50 USD kg^{-1} [32], and it is therefore critical that efficient use is made of the mass of 2D nanomaterials incorporated in a device. Comparing the gravimetric and areal capacitance of AMX electrodes with other high areal loading MXene-based electrodes across a wide range of scan rates (5 – 1000 mV s^{-1}) in Fig. 6a and b, the advantages of AMX electrodes become clear. The well-connected porous network of MXene thin films enables far greater retention of gravimetric capacitance, especially at high scan rates, when compared to other systems (Fig. 6a). This manifests in greater areal capacitance at scan rates of 200 mV s^{-1} and above, despite lower areal loading (Fig. 6b). For instance, while previously reported dense MXene electrodes initiated by hydroiodic acid (DMH-4, 58 mg cm^{-2}) [9], exhibit remarkable areal capacitance at low scan rates, they inefficiently use the active material at higher rates. This means just 78 F g^{-1} is measured at a relatively low rate of 100 mV s^{-1}. It should be noted, that the high gravimetric and areal capacitance figures of the AMX electrodes do not come at great expense of volumetric capacitance, despite the porous microstructure of the AMX electrodes, with performance being similar or only slightly lower than other systems, see Figure S 18a and b.

To additionally highlight the superior rate performance of AMX electrodes, they are compared at 200 mV s^{-1} in Fig. 6c and 6d to a wide range of supercapacitor electrode systems characterized by a similar areal loading and rate performance. This rate is chosen to correspond with a discharge time on the order of ~5 s (typical for supercapacitor applications) [30,31]. The AMX electrode materials show broadly superior areal and gravimetric performance, which is of particular note as typically, increased areal loadings are associated with better areal capacitance at the expense of gravimetric capacitance and therefore result in inefficient use of the active material.

Notable outliers are macroporous MXene (MP-Ti_3C_2) (0.43 mg cm^{-2}, 13 μm)[6] and hydrogel MXene (HG-Ti_3C_2) (11.3 mg cm^{-2}, 40 μm) [6], which exceed AMX electrodes in gravimetric capacitance and areal loading, respectively. These electrodes are analogous to AMX in their controlled microstructure in the case of MP-Ti_3C_2 (0.43 mg cm^{-2}, 13

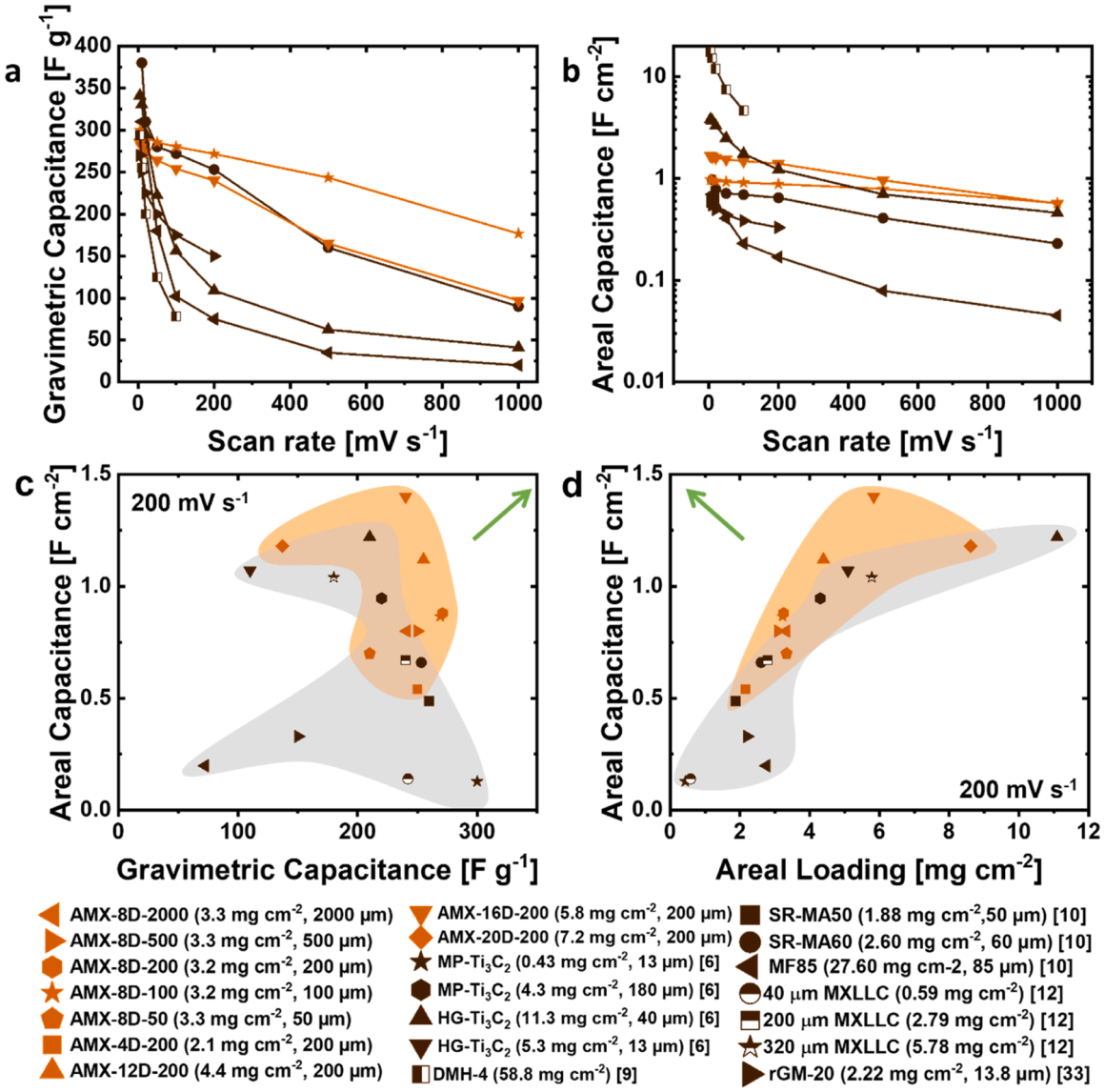

Fig. 6. (a) Gravimetric capacitance vs. scan rate of the 3D networked MXene thin films compared to other high areal loading electrode structures. (b) Areal capacitance vs. scan rate of the 3D networked MXene thin films compared to other high areal loading electrode structures. (c) Relationship between areal capacitance and gravimetric capacitance of the 3D networked MXene thin films compared to other electrode structures with comparable areal loading from literature at 200 mV s^{-1}. (d) Relationship between areal capacitance and areal loading of the 3D networked MXene thin films compared to these electrode structures from literature at 200 mV s^{-1}. [6,9,10,12,33].

μm) and nanostructure in the case of HG-Ti_3C_2 (11.3 mg cm^{-2}, 40 μm). However, the volumetric density is an additional important characteristic of the electrode because it affects volumetric and gravimetric capacitance simultaneously. As seen in Figure S 18c, the MP-Ti_3C_2 (0.43 mg cm^{-2}, 13 μm) electrode shows order of magnitude smaller areal capacitance than AMX at 200 mV s^{-1}, in return for a relatively modest improvement in gravimetric capacitance. Similarly, the volumetric density of HG-Ti_3C_2 (11.3 mg cm^{-2}, 40 μm) comes at the cost of gravimetric capacitance to the extent that the areal capacitance is comparable to that of AMX. This outstanding performance can be attributed to the well-controlled micro- and nanostructure of AMX electrodes. For additional clarity, comparisons of areal loading vs. gravimetric capacitance and areal loading vs. volumetric density for AMX electrodes and other electrode systems can be found in Figures S 18d and S 18e, respectively.

3. Device performance

To provide proof-of-concept device performance of AMX-based electrodes, a symmetric supercapacitor was prepared from AMX-8D-50 electrodes using 0.5 M H_2SO_4 electrolyte. Fig. 7a shows CV curves at different scan rates ranging from 5 to 500 mV s^{-1}.

The typical rectangular pattern of EDLC as well as peaks centered around 0.2 V attributable to $Ti_3C_2T_x$ pseudocapacitance are present. As the scan rate increases, the peaks shift to higher potentials for the oxidation and vice versa for the reduction processes. Gravimetric capacitance based on the mass of both electrodes vs. scan rate is shown in Fig. 7b, which decreases from 100 F g^{-1} at 5 mV s^{-1} to 44 F g^{-1} at 500 mV s^{-1}. Charge/discharge measurements are presented in Fig. 7c, showing the typical triangular profile of EDLC at high voltage, with minimal voltage drop due to internal resistance, as well as a slight plateau in the profile between 0 and 0.3 V, corresponding to the redox pseudocapacitance of the active material. Energy density was measured to be 8.8 Wh kg^{-1} at 0.2 kW kg^{-1} and 3.9 Wh kg^{-1} at 8.8 kW kg^{-1}. This compares favorably against other symmetric supercapacitors prepared using $Ti_3C_2T_x$ active material in conventional electrolytes [34–36]. Fig. 7d shows long-term cycling at 5 A g^{-1} for 10,000 cycles with good stability, retaining 84 % of the maximum capacitance, which was reached at 528 cycles.

4. Conclusion

In summary, we have shown how the micro- and nanostructure of 3D networked MXene thin films affect electrochemical performance and demonstrated a versatile and simple approach to improve both structural aspects using the same experimental approach. Well-aligned MXene layers are formed on a sacrificial scaffold by wet chemical assembly, resulting in a highly organized electrode structure with highly conductive electronic and ionic pathways. The 3D networked MXene thin films may be tuned in thickness from tens to hundreds of nanometers, leading to good accessibility of the individual MXene flakes and resulting in high gravimetric capacitance of 240 F g^{-1}, even at 200 mV s^{-1}. Second, controlled densification by up to 40 times compared to the initial state did not compromise the mechanical integrity of the electrodes and resulted in a high volumetric capacitance of up to 180 F cm^{-3}

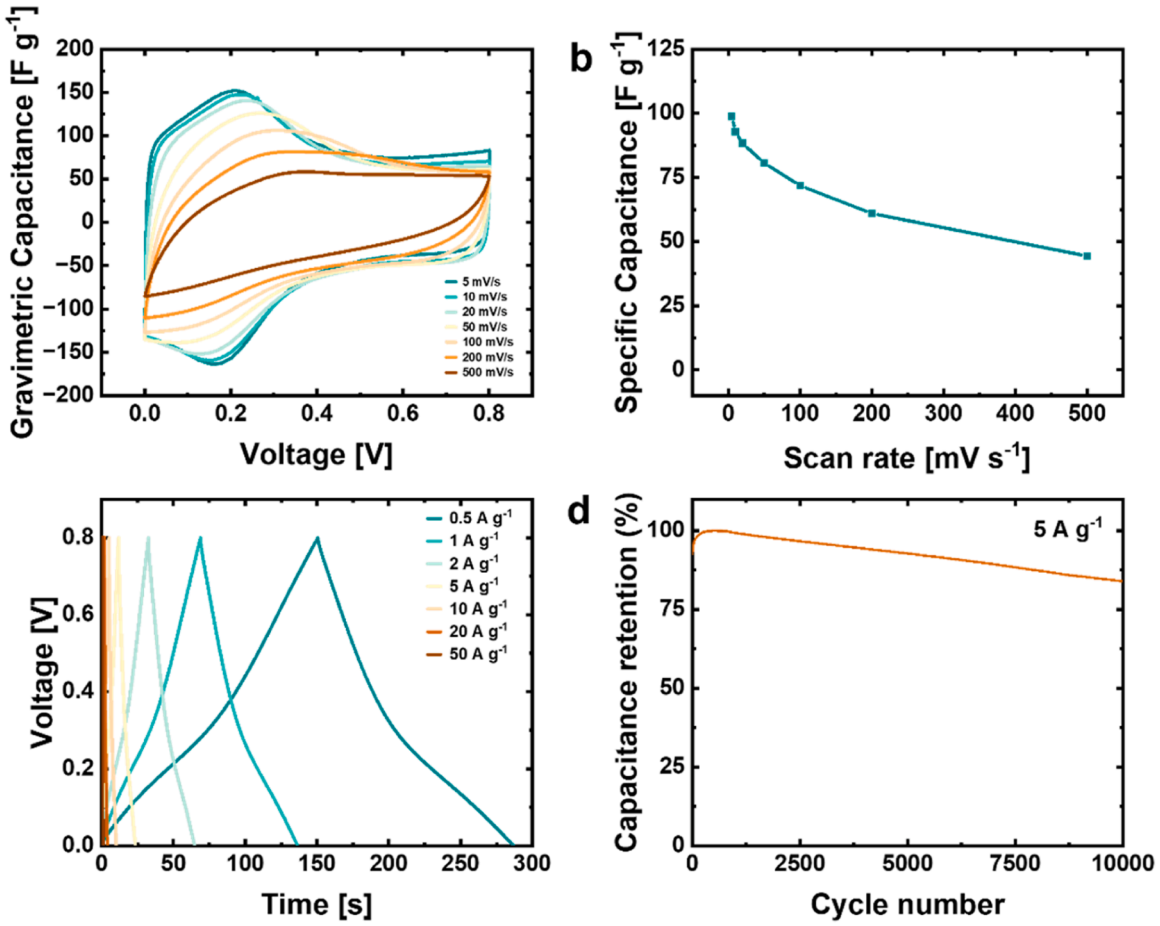

Fig. 7. (a) Cyclic voltammograms of a two-electrode device consisting of an AMX-8D-50 working electrode and AMX-8D-50 counter electrode at scan rates ranging from 5 to 100 mV s^{-1}. (b) Gravimetric capacitance based on the mass of both electrodes at scan rates from 5 to 500 mV s^{-1}. (d) Charge/discharge profile of a two-electrode AMX-8D-50 device at current densities of 0.5 to 50 A g^{-1}. d) Capacitance retention during long-term cycling at 5 A g^{-1} based on the peak capacitance reached.

at 50 mV s^{-1}. Furthermore, excellent areal capacitance of more than 1.4 F cm^{-2} at high scan rates of 200 mV s^{-1} was achieved. These unique properties mean that 3D networked MXene thin film electrodes compare favorably to other state-of-the-art supercapacitor electrodes when adopting a wholistic view of tunability as well as gravimetric, volumetric, and areal capacitance. This study clearly demonstrates the importance of thorough control over the nanometer- and micrometer-scale features of electrodes and opens new possibilities for application-grade supercapacitors.

5. Experimental Section

5.1. Synthesis of $Ti_3C_2T_x$

$Ti_3C_2T_x$ was synthesized from its parent MAX phase through a variation of the minimally intensive layer delamination (MILD) method [11, 37]. Deionized water (10 ml) was added to a vented PTFE vessel followed by drop-wise addition of concentrated hydrochloric acid (30 ml, Sigma). LiF powder (3.2 g, Sigma) and a magnetic PTFE stirrer bar was added, and the vessel was immersed in a mineral oil bath, stirring at 400 rpm for 10 min to fully dissolve the LiF and dissipate heat. Ti_3AlC_2 MAX phase powder (2 g, Carbon-Ukraine ltd.) was then added in small additions to the vessel over a period of 30 min to avoid overheating of the solution. The temperature was set to 35 °C and the vessel stirred at 400 rpm for 24 h to obtain multilayer $Ti_3C_2T_x$ MXene. The contents of the vessel were transferred evenly into four 50 ml centrifuge tubes and diluted to a total of 160 ml with deionized water. The dispersion was then sedimented *via* centrifugation at 5000 rpm using a Thermo Scientific Heraeus Multifuge X1 for 3 min, the supernatant was discarded, and sediments redispersed in deionized water. This was repeated several times, until the pH of the supernatant had reached at least 6. To delaminate, the contents of the tubes were transferred to a flask and stirred vigorously for a minimum of 2 h at 400 rpm. The dispersion was then centrifuged at 1500 rpm for 30 min to sediment any multi-layer MXene or unreacted MAX phase. The supernatant containing delaminated MXene flakes was then collected. This supernatant was concentrated *via* centrifugation at 5000 rpm for 1 hour. The sediments were redispersed in a minimal amount of deionized water to obtain a concentrated MXene ink with concentration greater than 30 mg/ml. To accurately determine the concentration of the MXene ink, 100 μl was transferred to a small glass vial and diluted with a 1:1 (v/v) ratio of deionized water and absolute ethanol (Fisher) before being filtered using a vacuum filtration funnel and pre-weighed 0.25 μm pore nitrocellulose filter membrane (Millipore VSWP). The vial and sides of the funnel were washed down with additional 1:1 deionized water and absolute ethanol. Once the filtration was complete the membrane and MXene filtride were dried overnight in a vacuum desiccator and then weighed to obtain the concentration of the ink.

5.2. Preparation of $Ti_3C_2T_x$ aeromaterial

For the preparation of 3D networked MXene thin film electrodes, tetrapodal ZnO (t-ZnO) particles, produced by a simple flame transport synthesis [38], were used as a sacrificial template material. The obtained t-ZnO powder is pressed into cylinders with a steel die (diameter = 12 mm, height = 2 mm) with a density of 0.3 g cm^{-3}. The cylinders were heat treated at 1150 °C for 5 h to obtain a freestanding and interconnected network. The prior obtained concentrated MXene ink was diluted to ~2 mg/ml using deionized water and probe sonicated at 30 % amplitude for 2 mins (Sonoplus, Bandelin) to achieve a well-mixed dispersion. Afterwards, the t-ZnO networks were saturated with the MXene dispersion and dried at 40 °C for 4 h in air to allow evaporation of the water. By repeated saturation and drying steps, the weight loading with MXene is adjusted. The final template was then treated in 1 M HCl (Carl Roth) overnight to fully etch the ZnO and rinsed with deionized water and absolute ethanol (99.99 %, Carl Roth) and finally dried using a critical point dryer (Leica EM CPD300).

5.3. Compression of $Ti_3C_2T_x$ aeromaterial

To tune the microstructure of the as-prepared AMX, the same steel die is use as for the preparation of the t-ZnO template. A spacer is used corresponding to the desired thickness: 50, 100, 200, 500, or 1000 μm. The AMX is then compressed slowly using manual pressure, with thickness determined by the spacer.

5.4. Preparation of 3D networked MXene thin film electrodes

The 3D networked MXene thin films were affixed to glass slides using 100 μl silver conductive paint (RS Pro) spread into an approximately 11 mm circle into which a doubled length of 0.1 mm silver wire was inserted (cf. Figure S 13b). The electrode was placed onto the paint and pressed gently to ensure adhesion but avoid deformation. The exposed silver wire was covered with Kapton tape (RS components) leaving sufficient length free at the end to connect a crocodile clip. The paste was dried in ambient conditions for 1 hour before being placed in a vacuum desiccator for a minimum of 2 h to fully dry the silver paint.

5.5. Preparation of $Ti_3C_2T_x$ symmetric supercapacitor devices

3D networked MXene thin film structures (AMX-8D-50) were used as both negative and positive electrodes, cut to a diameter of 3 mm. Both electrodes were pre-soaked with 0.5 M H_2SO_4 and were assembled in Swagelok cells with glassy carbon electrodes using a pre-soaked glass fiber filter (Whatman) as a separator.

5.6. Electrochemical measurements

All electrochemical measurements were carried out with a VMP-300 potentiostat (BioLogic S.A.). The electrochemical cell, as seen in Figure S 13a was configured with the as-prepared $Ti_3C_2T_x$ electrode as the working electrode, an oversized glassy carbon rod as the counter electrode, and an Ag/AgCl reference (SI Analytics). The electrolyte used was 0.5 M H_2SO_4. A potential window of −0.65 to 0.2 V was chosen for the measurements, which consisted briefly of cyclic voltammetry (CV) from 5 mV s^{-1} to 1000 mV s^{-1}; galvanostatic cycling with potential limitation (GCPL) with current density from 2 to 100 A g^{-1}; potentiostatic electrochemical impedance spectroscopy (PEIS) from 10 mHz to 100 kHz, and long term GCPL for 5000 cycles at a current density of 10 A g^{-1}. Samples were pre-cycled before the above set of measurements using CV at 50 mV s^{-1} for 300 cycles. This was to allow full wetting of the electrodes, especially in the case of the highly compressed samples.

Electrochemical characterization of the $Ti_3C_2T_x$ symmetric devices was performed using a VMP-300 potentiostat (BioLogic S.A.). A potential window of 0 to 0.8 V was used for the measurements, which consisted of CVs from 5 to 500 mV s^{-1}, GCPL at current densities from 0.5 to 50 A g^{-1}, and with a current density of 5 A g^{-1} for 10,000 cycles for long term stability testing. Gravimetric capacitance was calculated using the total mass of the two electrodes and not subject to any normalization factor.

5.7. Capacitance calculations

Specific capacitance for each electrode was calculated using the discharge portion of the fourth CV curve according to the following equation:

$$C \Big/ m = \frac{1}{m_e \upsilon \Delta V} \int_{-0.65}^{0.2} i dV$$

Where $C\,m^{-1}$ is the specific capacitance (F g^{-1}), i is the current (mA), V is

the potential (V), m_e is the electrode mass (g), υ is the scan rate (mV s^{-1}) and ΔV is the potential window (V).

The volumetric capacitance was calculated in the same manner according to the following equation:

$$C \Big/ V = \frac{1}{V_e \upsilon \Delta V} \int_{-0.65}^{0.2} idV$$

Where $C\,V^{-1}$ is the specific capacitance (F cm^{-3}), i is the current (mA), V is the potential (V), V_e (cm^{-3}) is the volume of the electrode defined by the area of the template used (cm^{-2}) and the thickness determined by SEM (cm), υ is the scan rate (mV s^{-1}) and ΔV is the potential window (V).

5.8. Characterization of structure and properties

The structure and morphology of the prepared materials were characterized by scanning electron microscopy using a Zeiss Supra 55VP operated at 2 kV.

The nanostructure of both MXene covered ZnO templates as well as free-standing AMX structure was analyzed by transmission electron microscopy (TEM) with a FEI Tecnai F30 G^2 at 300 kV acceleration voltage. In order to obtain separated tetrapods a small amount of material was ground in butanol and drop coated onto lacey carbon TEM grids. The chemical composition of single tubes of the AMX material is analyzed via energy dispersive x-ray spectroscopy (EDX, EDAX Si-Li detector) in the TEM. The wall thickness of single AMX tetrapod arms / tubes is determined via the electron energy loss spectroscopy (EELS) log ratio method [39].

The thickness in electron beam direction can be determined in multiples of the electron mean free path (eMFP) by comparing the integrated intensity of the zero-loss peak to the total integrated intensity (see Figure S 10) in the case of inelastic scattering. A scanning TEM (STEM) EELS line scan over the width of an AMX tube yields an eMFP thickness profile. Taking an average of the center region, multiplying with a suitable value of the eMFP for the $Ti_3C_2T_x$ MXene material and dividing by a factor of 2 (due to two layers being penetrated by the electron beam) then gives the wall thickness of the aeromaterial. Values for the eMFP can be calculated via an estimation given in [39] or [40]. Multiple tubes and positions are measured for each amount of areal loading.

Data availability

The data that support the plots within this paper and other findings of this study are available from the corresponding authors on request.

CRediT authorship contribution statement

Dahnan Spurling: Conceptualization, Methodology, Validation, Formal analysis, Investigation, Writing – original draft, Writing – review & editing. **Helge Krüger:** Conceptualization, Methodology, Validation, Formal analysis, Investigation, Writing – original draft, Writing – review & editing. **Niklas Kohlmann:** Methodology, Validation, Formal analysis, Investigation, Writing – original draft, Writing – review & editing. **Florian Rasch:** Conceptualization, Methodology, Writing – review & editing. **Matthias P. Kremer:** Conceptualization, Methodology, Writing – review & editing. **Lorenz Kienle:** Writing – review & editing. **Rainer Adelung:** Conceptualization, Methodology, Writing – review & editing, Visualization, Supervision, Project administration, Funding acquisition. **Valeria Nicolosi:** Conceptualization, Methodology, Writing – original draft, Writing – review & editing, Visualization, Supervision, Project administration, Funding acquisition. **Fabian Schütt:** Conceptualization, Methodology, Writing – original draft, Writing – review & editing, Visualization, Supervision, Project administration, Funding acquisition.

Declaration of competing interest

The authors declare that they have no known competing financial interests or personal relationships that could have appeared to influence the work reported in this paper.

Acknowledgments

VN wishes to thank the support from of the ERC CoG 3D2DPrint, the SFI AMBER and I-Form Centres and the SFI Future Frontiers Programme. DS and VN thank the support from the IRC and Intel EPS Grant (EPSPG 207342). FS, RA and VN acknowledge funding by the EIC project SuperHeart. LKacknowledges funding by the Deutsche Forschungsgemeinschaft (DFG) under contract KI 1263/17–1. This project has received funding from the European Union's Horizon 2020 Research and Innovation Programme under grant agreement No GrapheneCore3 881603.

Supplementary materials

Supplementary material associated with this article can be found, in the online version, at doi:10.1016/j.ensm.2023.103148.

References

[1] U.S. Department of Energy, Energy storage grand challenge energy storage market report 2020, *U.S. Depart. Energy* Technical 65 (2020).
[2] P. Simon, Y. Gogotsi, Materials for electrochemical capacitors, Mater. Sustain. Energy (2010) 138–147, https://doi.org/10.1142/9789814317665_0021.
[3] Y. Wang, et al., Supercapacitor devices based on graphene materials, J. Phys. Chem. C 113 (2009) 13103–13107.
[4] P. Kossyrev, Carbon black supercapacitors employing thin electrodes, J. Power Sources 201 (2012) 347–352.
[5] X. Zhang, Z. Zhang, Z. Zhou, MXene-based materials for electrochemical energy storage, J. Energy Chem. 27 (2018) 73–85.
[6] M.R. Lukatskaya, et al., Ultra-high-rate pseudocapacitive energy storage in two-dimensional transition metal carbides, Nat Energy 6 (2017) 1–6.
[7] H. Sun, et al., Hierarchical 3D electrodes for electrochemical energy storage, Nat. Rev. Mater. 4 (2019) 45–60.
[8] S.H. Park, et al., High areal capacity battery electrodes enabled by segregated nanotube networks, Nat. Energy 4 (2019) 560–567.
[9] Z. Wu, et al., Hydroiodic-acid-initiated dense yet porous Ti3C2Tx MXene monoliths toward superhigh areal energy storage, Adv. Mater. 2300580 (2023) 1–8.
[10] V. Bayram, et al., MXene tunable lamellae architectures for supercapacitor electrodes, ACS Appl Energy Mater 3 (2020) 411–422.
[11] M. Ghidiu, M.R. Lukatskaya, M.Q. Zhao, Y. Gogotsi, M.W. Barsoum, Conductive two-dimensional titanium carbide 'clay' with high volumetric capacitance, NatureNature 516 (2015) 78–81.
[12] Y. Xia, et al., Thickness-independent capacitance of vertically aligned liquid-crystalline MXenes, NatureNature 557 (2018) 409–412.
[13] M. Alhabeb, et al., Guidelines for synthesis and processing of two-dimensional titanium carbide (Ti3C2Tx MXene), Chem. Mater. 29 (2017) 7633–7644.
[14] M. Shekhirev, C.E. Shuck, A. Sarycheva, Y. Gogotsi, Characterization of MXenes at every step, from their precursors to single flakes and assembled films, Prog. Mater Sci. 120 (2021) 100757.
[15] F. Rasch, et al., Wet-chemical assembly of 2D nanomaterials into lightweight, microtube-shaped, and macroscopic 3D networks, ACS Appl. Mater. Interfaces 11 (2019) 44652–44663.
[16] M. Mecklenburg, et al., Aerographite: ultra lightweight, flexible nanowall, carbon microtube material with outstanding mechanical performance, Adv. Mater. 24 (2012) 3486–3490.
[17] F. Schütt, et al., Hierarchical self-entangled carbon nanotube tube networks, Nat. Commun. 8 (2017) 1–10.
[18] R. Meija, et al., Nanomechanics of individual aerographite tetrapods, Nat. Commun. 8 (2017) 1–9.
[19] K. Chen, et al., MXene-derived C-doped TiO2/Ti3C2 heterojunction as a high-performance visible-light photocatalyst, Res. Chem. Intermed. 48 (2022) 4443–4458.
[20] X. Zhao, et al., pH, nanosheet concentration, and antioxidant affect the oxidation of Ti3C2Tx and Ti2CTx MXene dispersions, Adv. Mater. Interfaces 7 (2020) 1–11.
[21] A. Sarycheva, Y. Gogotsi, Raman spectroscopy analysis of the structure and surface chemistry of Ti3C2T xMXene, Chem. Mater. 32 (2020) 3480–3488.
[22] H. Meltzman, et al., An experimental method for calibration of the plasmon mean free path, J. Microsc. 236 (2009) 165–173.
[23] H. Shao, et al., Unraveling the charge storage mechanism of Ti3C2Tx MXene electrode in acidic electrolyte, ACS Energy Lett. 5 (2020) 2873–2880.

[24] K. Maleski, C.E. Ren, M.Q. Zhao, B. Anasori, Y. Gogotsi, Size-dependent physical and electrochemical properties of two-dimensional MXene flakes, ACS Appl. Mater. Interfaces 10 (2018) 24491–24498.
[25] J. Wu, X.Z. Yuan, H. Wang, Cyclic voltammetry, PEM Fuel Cell Diagnostic Tools (2011) 71–85, https://doi.org/10.1201/9781439807842.ch10.
[26] T. Tichter, J. Schneider, C. Roth, Convolutive modeling of cyclic voltammetry, AC-voltammetry, sine wave voltammetry and impedance spectroscopy with interfacial CPE behaviour and uncompensated ohmic resistances: a unified theory, Electrochim. Acta 393 (2021) 139006.
[27] D.M. MacArthur, The proton diffusion coefficient for the nickel hydroxide electrode, J. Electrochem. Soc. 117 (1970) 729.
[28] H. Lindström, et al., Li+ ion insertion in TiO2 (anatase). 1. Chronoamperometry on CVD films and nanoporous films, J. Phys. Chem. B 101 (1997) 7710–7716.
[29] J. Wang, J. Polleux, J. Lim, B. Dunn, Pseudocapacitive contributions to electrochemical energy storage in TiO 2 (anatase) nanoparticles, J. Phys. Chem. C 111 (2007) 14925–14931.
[30] Eyer, J., Corey, G.P. & SANDIA. Energy storage for the electricity grid: benefits and market potential assessment guide. A study for the DOE energy storage systems program 232 (2010).
[31] F. Rafik, H. Gualous, R. Gallay, A. Crausaz, A Berthon, Frequency, thermal and voltage supercapacitor characterization and modeling, J. Power Sources 165 (2007) 928–934.
[32] Y. Wang, J. Wang, X. Zhang, D. Bhattacharyya, E.M. Sabolsky, Quantifying environmental and economic impacts of highly porous activated carbon from lignocellulosic biomass for high-performance supercapacitors, Energies 15 (2022).
[33] Y. Luo, et al., Micro-structural and flexible reduced graphene Oxide/Ti3C2Tx composite film electrode with long cycle life for supercapacitor, Adv. Mater. Interfaces 9 (2022) 2101619.
[34] Y. Tian, et al., Understanding MXene-based 'symmetric' supercapacitors and redox electrolyte energy storage, ACS Appl. Energy Mater 3 (2020) 5006–5014.
[35] B. Guo, et al., A binder-free electrode based on Ti3C2Tx-rGO aerogel for supercapacitors, Colloids Surf. Physicochem. Eng. Asp 595 (2020) 124683.
[36] Z. Liu, et al., A Ti3C2TX@PEDOT composite for electrode materials of supercapacitors, J. Electroanal. Chem. 881 (2021) 114958.
[37] X. Sang, et al., Atomic defects in monolayer titanium carbide (Ti3C2Tx) MXene, ACS Nano 10 (2016) 9193–9200.
[38] Y.K. Mishra, et al., Fabrication of macroscopically flexible and highly porous 3D semiconductor networks from interpenetrating nanostructures by a simple flame transport approach, Part. Part. Syst. Char. 30 (2013) 775–783.
[39] T. Malis, S.C. Cheng, R.F. Egerton, EELS log-ratio technique for specimen-thickness measurement in the TEM, J. Electron Microsc. Tech. 8 (1988) 193–200.
[40] K. Iakoubovskii, K. Mitsuishi, Y. Nakayama, K. Furuya, Thickness measurements with electron energy loss spectroscopy, Microsc. Res. Tech. 71 (2008) 626–631.